Electrocatalysis Hot Paper

Deutsche Ausgabe: DOI: 10.1002/ange.201509758
Internationale Ausgabe: DOI: 10.1002/anie.201509758

Interacting Carbon Nitride and Titanium Carbide Nanosheets for High-Performance Oxygen Evolution

*Tian Yi Ma[+], Jian Liang Cao[+], Mietek Jaroniec, and Shi Zhang Qiao**

Abstract: *Free-standing flexible films, constructed from two-dimensional graphitic carbon nitride and titanium carbide (with MXene phase) nanosheets, display outstanding activity and stability in catalyzing the oxygen-evolution reaction in alkaline aqueous system, which originates from the Ti–N_x motifs acting as electroactive sites, and the hierarchically porous structure with highly hydrophilic surface. With this excellent electrocatalytic ability, comparable to that of the state-of-the-art precious-/transition-metal catalysts and superior to that of most free-standing films reported to date, they are directly used as efficient cathodes in rechargeable zinc–air batteries. Our findings reveal that the rational interaction between different two-dimensional materials can remarkably promote the oxygen electrochemistry, thus boosting the entire clean energy system.*

Developing highly efficient and cost-effective electrocatalysts for the oxygen-evolution reaction (OER) is of great significance, since the OER is coupled with key clean energy systems like electrolytic/solar water splitting and rechargeable metal–air batteries.[1,2] However, the prohibitive costs and scarcity of the precious metals used as OER catalysts (e.g. IrO_2, RuO_2) limit the large-scale commercialization of these technologies.[3] Thus, extensive efforts have been directed to non-precious-metal catalysts (NPMCs),[4,5] in which metal–nitrogen–carbon (Me-N-C) materials are particularly attractive because of their excellent electroactivity, strong durability, and easy fabrication, and the transition metals promoted by N ligation forming Me–N_x species are widely assumed to boost oxygen electrochemistry.[6–8] They are prepared by pyrolysis of precursors comprising transition metals and *N*-containing ligands (on conductive carbon supports if necessary), resulting in metal centers coordinated by macrocycles (e.g. phthalocyanine),[9] polymers (e.g. polyaniline),[10,11] or graphitic structures (e.g. N-doped carbon nanotubes).[12,13] However, thermolysis at high temperature is required, which results in powdery catalysts needing complex post-processing before their use in real devices.

Recently a new family of two-dimensional (2D) layered metal carbides/carbonitrides, labeled as MXene to underline its similarity to graphene, has triggered great research enthusiasm. It is synthesized by etching of A from the MAX phase ($M_{n+1}AX_n$, where M denotes early transition metal, A denotes a main group 3 or main group 4 element, and X denotes C or N),[14,15] for example, titanium carbide (Ti_3C_2) derived from Ti_3AlC_2. MXene materials possess a hydrophilic surface, excellent electrical conductivity, and good structural/chemical stability,[16,17] an uncommon combination that is highly promising for electrocatalysis. Sonication-assisted exfoliation of MXene produces the single-layer and few-layer nanosheets, which can further yield free-standing films through filtration,[15,17] cold pressing,[16] or rolling.[14] In spite of the rich chemistry and unique morphology of MXene, its applications are restricted to supercapacitors and lithium-ion batteries for electricity storage.[14–17] On the other hand, graphitic carbon nitrides (g-C_3N_4) with ultrahigh N content, stable and tailorable 2D layered structures[18–20] have been widely investigated as the host for metal species, showing outstanding electrocatalytic and photoelectrocatalytic activity,[21–23] which originates from the interaction between the N-rich network and metal centers. Therefore, coupling g-C_3N_4 and MXene for high-performance electrocatalysis is expected by taking advantage of their similar 2D geometry and Me-N_x interaction between them.

Herein, the hybrid film (TCCN) of overlapped g-C_3N_4 and Ti_3C_2 nanosheets is designed as a highly efficient oxygen electrode. Ti_3C_2 is coupled with g-C_3N_4 through Ti-N_x interaction, forming a porous free-standing film with hydrophilic surface and conductive framework, which exhibits excellent performance in catalyzing the OER and in Zn–air batteries.

The TCCN film was prepared by homogeneous assembly of Ti_3C_2 and g-C_3N_4 nanosheets (Figure 1 a). Dense Ti_3AlC_2 particles (MAX) were first etched by HF to extract Al species, generating Ti_3C_2 (MXene) with a loosely packed accordion-like structure as observed by scanning electron microscopy (SEM, Figures S1 a–c and S2 in the Supporting Information). Disappearance of the most intense diffraction peak of Ti_3AlC_2 at 39° (2θ) and the shift of (00l) peaks, for example, (002) and (004), to lower angles on the X-ray diffraction (XRD) patterns indicate the transformation of Ti_3AlC_2 to Ti_3C_2 (Figure 1 b).[14,15] The obtained Ti_3C_2 was mixed with bulk g-C_3N_4, then subjected to sonication-assisted exfoliation, during which homogeneously blended g-C_3N_4 and Ti_3C_2 nanosheets were obtained by breaking the weakened interlayer inter-

[*] Dr. T. Y. Ma,[+] Prof. S. Z. Qiao
School of Chemical Engineering, The University of Adelaide
Adelaide, SA 5005 (Australia)
E-mail: s.qiao@adelaide.edu.au
Prof. J. L. Cao[+]
School of Materials Science and Engineering
Henan Polytechnic University, Henan, Jiaozuo 454000 (China)
Prof. M. Jaroniec
Department of Chemistry and Biochemistry
Kent State University, Kent, OH 44240 (USA)
[+] These authors contributed equally to this work.
Supporting information and ORCID(s) from the author(s) for this article are available on the WWW under http://dx.doi.org/10.1002/anie.201509758.

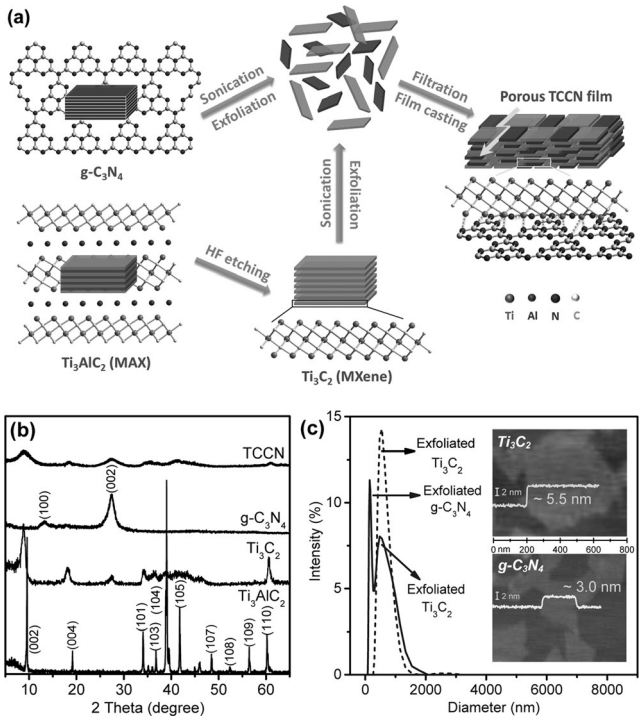

Figure 1. a) Fabrication of the porous TCCN film. b) XRD patterns of Ti_3AlC_2, Ti_3C_2, g-C_3N_4, and TCCN. c) Particle size distributions of the Ti_3C_2 dispersion and the mixed dispersion of Ti_3C_2 and g-C_3N_4 after exfoliation. inset in panel c) AFM images of exfoliated Ti_3C_2 and g-C_3N_4 nanosheets.

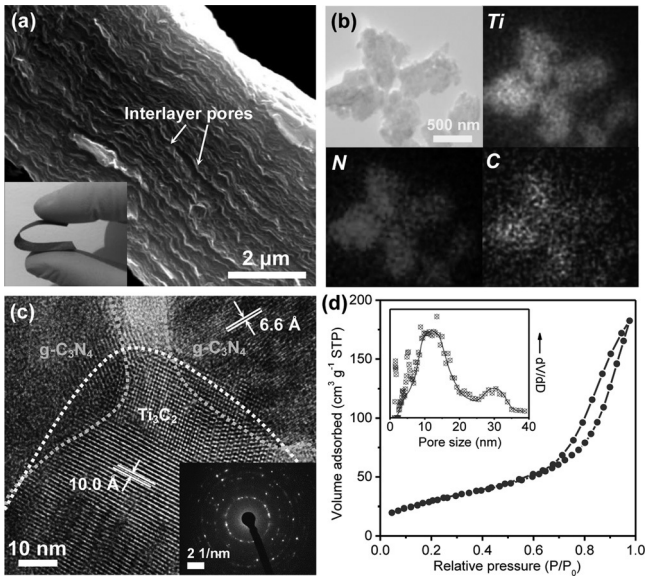

Figure 2. a) SEM, inset in panel a) optical, b) EDS elemental mapping, c) HRTEM images, and inset in panel c) SAED pattern of TCCN. d) N_2 adsorption isotherm, and inset in panel d) the corresponding differential pore size distribution for TCCN.

actions (e.g. hydrogen bonds) in their bulk phases.[16,24] The successful exfoliation of Ti_3C_2 and g-C_3N_4 is first revealed by the nanosheet morphology observed by SEM (Figure S1 d–f) and AFM (Figure 1 c inset) imaging, showing a thickness of 5.5 and 3.0 nm, respectively. It is also evidenced by the formed stable colloidal solution with obvious Tyndall scattering effect (Figure S3), in which the peaks at 580 and 170 nm in the particle size distribution curves are ascribed to the exfoliated Ti_3C_2 and g-C_3N_4, respectively (Figure 1 c). Driven by the subsequent directional flow caused by vacuum suction, mixed Ti_3C_2 and g-C_3N_4 nanosheets were prone to the layer-by-layer self-assembly on the filter membrane surface to afford a hybrid film.[25] Characteristic structural features of Ti_3C_2 are evident in TCCN as shown by the well-preserved diffraction peaks from MXene (Figure 1 b), while the incorporation of g-C_3N_4 is verified by the CN graphitic-like interlayer diffraction peak at 27.5° (2θ).[18–20]

TCCN is a highly flexible macroscopic film of a few centimeters in size and 8–10 μm in thickness (Figure 2 a, Figure S4). The oriented assembly of g-C_3N_4 and Ti_3C_2 nanosheets affords plenty of interlayer large pores ranging from tens to hundreds of nanometers. The uniform dispersion of Ti, N, and C elements (energy dispersive X-ray spectroscopy (EDS) elemental mapping images, Figure 2 b) verifies a homogeneous assembly of g-C_3N_4 and Ti_3C_2 in TCCN, which agrees well with the X-ray photoelectron spectroscopy (XPS, Figure S5), showing Ti (25.8 atm %), C (31.2 atm %) and N (13.7 atm %). The high-resolution transmission electron microscopy (HRTEM) with the selected-area electron diffraction pattern (SAED) reveals two overlapped crystalline domains of g-C_3N_4 and Ti_3C_2 (Figure 2 c). N_2 adsorption analysis confirms the high surface area (205 $m^2 g^{-1}$) of TCCN and bimodal pore size distribution with two peaks located at 13 and 31 nm (Figure 2 d), matching well with the mesopores and interlayer large pores observed by SEM imaging.

TCCN can be directly used as the working electrode for the OER (Figure S6, Movie S1). In the polarization curves (Figure 3 a), both g-C_3N_4 and Ti_3C_2 show very low OER response, while the anodic current recorded on TCCN renders a sharp onset potential at 1.44 V versus reversible hydrogen electrode (RHE) with greatly enhanced OER current, indicating that the coupling of g-C_3N_4 and Ti_3C_2 can significantly improve the catalytic activity. Noticeably, the OER current of TCCN even exceeds that of IrO_2/C (20 wt % IrO_2 supported on carbon powder, see synthesis in the Supporting Information) at potentials beyond 1.54 V. By comparing the operating potential to deliver a 10.0 mA cm^{-2} current density ($E_{j=10}$), it is found that under the same experimental conditions in 0.1 M KOH aqueous media, TCCN displays an $E_{j=10}$ value of 1.65 V, lower than that of IrO_2/C (1.70 V), comparable or even better than those of the state-of-the-art precious-metal catalysts (e.g. RuO_2,[26] 1.73 V), transition-metal catalysts (e.g. $Mn_3O_4/CoSe_2$,[27] 1.68 V; Mn_xO_y/N-doped carbon,[28] 1.68 V), and previously reported OER catalysts with the same free-standing film configuration (e.g. $NiCo_2O_4$-graphene film,[29] 1.69 V; g-C_3N_4-graphene film,[30] 1.65 V; N-doped graphene-carbon nanotube film,[31] 1.70 V). A detailed comparison of highly active OER catalysts with various chemical compositions and different electrode structures demonstrates that TCCN is among the most efficient OER electrocatalysts reported so far (Table S1).

The Tafel slope of TCCN (74.6 mV $decade^{-1}$) is lower than that of IrO_2/C (93.2 mV $decade^{-1}$), Ti_3C_2 (119.7 mV de-

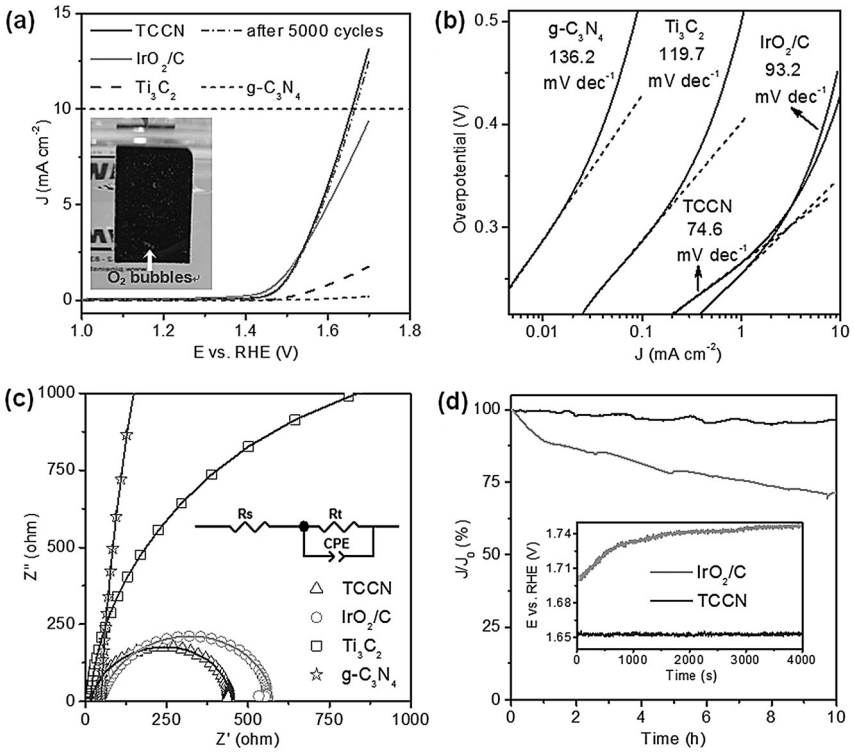

Figure 3. a) Polarization curves, b) Tafel plots, and c) EIS (recorded at 1.60 V with inset showing the equivalent circuit diagram) of TCCN, IrO_2/C, Ti_3C_2, and g-C_3N_4 in an O_2-saturated 0.1 M KOH solution (scan rate: 0.5 $mV s^{-1}$). Inset in panel a) optical image of TCCN directly used as the OER electrode operating at 1.70 V with generated bubbles on the surface indicating the formation of O_2 gas. Dash line in panel a) Polarization curve of TCCN after 5000 potential cycles (scan rate: 100 $mV s^{-1}$). d) Chronoamperometric response at a constant potential of 1.65 V ($E_{j=10}$ of TCCN), and inset in panel d) chronopotentiometric response at a constant current density of 10.0 $mA cm^{-2}$ of TCCN as compared to that of IrO_2/C.

cade^{-1}), g-C_3N_4 (136.2 mV decade^{-1}, Figure 3b), and comparable to that of reported highly active OER catalysts (Table S1), indicating its favorable reaction kinetics. This is also implied by the electrochemical impedance spectroscopy (EIS, Figure 3c), in which the semicircle diameter of TCCN is much smaller than that of the control group of catalysts because of the lower contact and charge transfer impedance in TCCN consisting of strongly coupled conductive Ti_3C_2 and g-C_3N_4. Furthermore, by employing the rotating ring-disk electrode (RRDE) technique (Figure S7), the OER process occurring on TCCN is confirmed to be dominated by a desirable four-electron pathway with negligible peroxide intermediate formation ($4OH^- \rightarrow O_2 + 2H_2O + 4e^-$) and a high Faradaic efficiency of 95.5%.

The chronoamperometric response reveals the high stability of TCCN, showing a slight anodic current attenuation of 4.3% (Figure 3d) with no phase or morphology change of the electroactive species after 10 h reaction (Figure S8), whereas IrO_2/C displays a current attenuation of 29.7% (7 times larger than TCCN). This indicates the apparent advantage of the free-standing films as compared to the post-coated powdery catalysts on electrode substrates, because the latter suffer from peeling off during the evolution of a large amount of O_2 gas.[1–3] In the chronopotentiometric response, TCCN affords a nearly constant $E_{j=10}$ of 1.65 V (Figure 3d inset), whereas $E_{j=10}$ of IrO_2/C increases for >40 mV within 4000 s. Also, only 4.5% anodic current loss is observed for TCCN after 5000 continuous potential cycles at an accelerated scanning rate of 100 $mV s^{-1}$ (dashed line in Figure 3a), suggesting TCCN is also highly stable to withstand accelerated degradation. Further experiments confirm the effective operation of TCCN in concentrated electrolytes such as 1.0 M KOH solution (Figure S9).

To gain an insight into the catalytic mechanism, a hybrid film (TCG) of Ti_3C_2 and graphene was prepared by the same method to that of TCCN (see synthesis in Supporting Information). Graphene was used to replace g-C_3N_4, because it also has a 2D layered structure similar to that of g-C_3N_4 nanosheets, but without N ligands. However, TCG shows apparently inferior activity and reaction kinetics (onset potential of 1.47 V, Tafel slope of 108.9 mV decade^{-1}, Figure 4a). To figure out the origin of this big difference, XPS analysis was first conducted, in which the Ti 2p profile of TCCN shifts noticeably to higher binding energy region in comparison to that of TCG and pure Ti_3C_2, for example, Ti-C $2p_{3/2}$ from 455.0 eV to 455.9 eV (Figure 4b and Figure S10). It reveals that the interaction of Ti with g-C_3N_4 impairs the electron density of Ti atoms, which can facilitate the adsorption of OH^- in alkaline media, promoting the electron transfer for an earlier O_2 evolution.[32,33] Correspondingly, the dominant peak at 398.5 eV of triazine rings (C=N–C)[18] in the N 1s spectrum of TCCN splits to form a new shoulder peak at 397.4 eV (Figure 4c), caused by the coupling of N in g-C_3N_4 with Ti_3C_2.[34,35] Similarly, the N K-edge synchrotron-based near-edge X-ray absorption fine structure (NEXAFS) of pure g-C_3N_4 shows two typical π* resonances at 399.8 and 402.5 eV from N in C=N–C and N(-C)$_3$ moieties, respectively (Figure 4d),[19,20] while a decreased intensity of the two resonances and a slight shift of π* resonance of C = *N*-C coordination from 399.8 to 399.5 eV are observed for TCCN. This is also due to the interaction between g-C_3N_4 and Ti_3C_2, leading to the perturbations of N atoms.[21–23] Thus, a combination of NEXAFS and XPS data implies the most probable interfacial Ti–N_x interaction model of TCCN (Figure 4d inset), which assumes the presence of highly dispersed active sites,[11] endowing TCCN superior OER activity.

The novel electrode structure of TCCN also contributes to its excellent performance. First, the free-standing film with hierarchical pores affords a high electrochemical double layer capacitance (C_{dl}), which is proportional to the active surface area. The C_{dl} of TCCN was confirmed to be 29.7 mF cm^{-2}, nearly 3 times higher than that of powdery TCCN (ball-milled TCCN to destroy the film and associated porosity, C_{dl} =

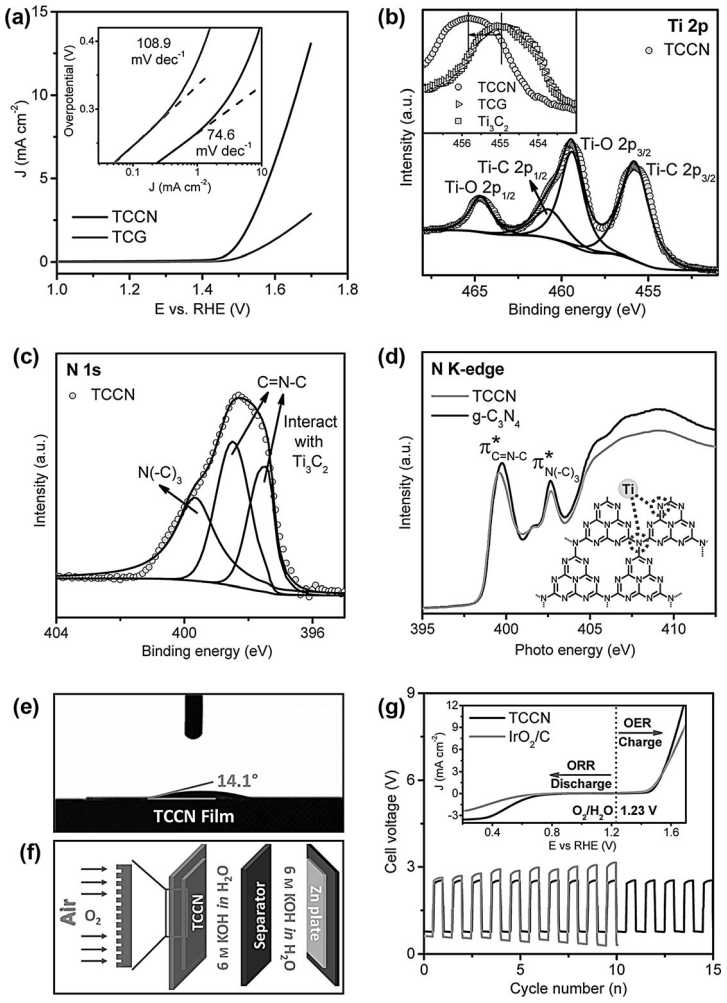

Figure 4. a) Polarization curves, and inset in panel a) Tafel plots of TCCN and TCG. High-resolution XPS spectra of b) Ti 2p and c) N 1s core levels in TCCN. Inset in panel b) Comparison of Ti-C $2p_{3/2}$ positions of TCCN, TCG, and Ti_3C_2. d) N K-edge NEXAFS of TCCN and g-C_3N_4 with inset showing the relative N sites. e) Contact angle of the TCCN film. f) Schematic configuration of a Zn–air battery. g) Charge–discharge cycling curves of Zn–air batteries using the TCCN film and IrO_2/C powder coated on GDL as the air cathode, respectively. Inset in panel g) Polarization curves of the TCCN film and IrO_2/C powder tested by using the three-electrode system in the whole OER/ORR region in O_2-saturated 0.1 M KOH solution.

10.3 mF cm^{-2}; Figures S11 and S12). It demonstrates that the free-standing porous films are more effective in enlarging the catalytically active surface area than conventional powdery catalysts post-coated on substrates. Unsurprisingly, the TCCN film delivers a much higher current density than that of powdery TCCN (e.g. 13 mV cm^{-2} versus 4 mV cm^{-2} at 1.70 V; Figures S13 and S14). Second, the easy peeling of the post-coated powdery catalysts during OER that involves continuous O_2 evolution greatly impairs their activity and life time.[3–5] In the TCCN film, no polymeric binders or conductive additives are employed, consequently reducing the dead volume and undesirable interface and eliminating the associated overpotentials,[29–31] which is evidenced by the higher OER activity and stronger durability of the TCCN film than those of powdery IrO_2/C (Figure 3, Figure S9) and powdery TCCN (Figure S13). Notably, operating at a high potential of 1.80 V, the TCCN film shows no visible peeling off even after 5 h reaction or in a highly bent form (Movie S1). Third, because of the hydroxy or oxygen-terminated surface, TCCN is highly hydrophilic with a small contact angle of 14.1° (Figure 4e), which is favorable for using aqueous electrolytes in energy storage/conversion devices.[14,15] The highly hydrophilic nature endows TCCN with excellent wettability in aqueous solutions (Figure S15), facilitating access of the electrolyte to the active surface of the film. Meantime, the hierarchical pores in TCCN provide smooth pathway for quick transfer of reactants (e.g. OH^-) in the electrolyte to the active sites, as well as for the fast emission of reaction products (e.g. O_2).

A proof-to-concept test was conducted to demonstrate TCCN's feasibility in real rechargeable Zn–air batteries by directly using it as the air cathode (Figure 4f). In polarization curves of the assembled coin-type Zn–air battery (Figure S16), TCCN afforded a current density of 20 mA cm^{-2} at 0.87 and 2.55 V for discharging (ORR) and charging (OER), respectively, largely outperforming those of powdery IrO_2/C coated on the gas diffusion layer (GDL) as the cathode (0.61 and 2.70 V). This is consistent with polarization curves recorded by using the three-electrode system, in which TCCN can not only catalyze OER, but also stably catalyze the reverse ORR through a four-electron pathway (Figure 4g inset and Figure S17). More importantly, TCCN displays no obvious potential fluctuation for over 15 pulse cycles, whereas an apparent overpotential increase for both discharging and charging processes is observed after five cycles for IrO_2/C (Figure 4g), because of the instability of the precious metal, as well as the deterioration of the carbonaceous GDL and the polymeric binder used for powder coating.[3,19]

In summary, the porous TCCN film performs as a flexible oxygen electrode with high activity and strong durability. The self-supported and binder-free configuration allows its direct use in rechargeable Zn–air batteries. This work will pave the way to a large variety of hybrid catalysts by coupling different 2D materials through the strong interactions between them, creating new opportunities for the R&D of clean energy system.

Acknowledgements

This work is financially supported by the Australian Research Council (ARC) through the Discovery Project programs (grant numbers DP140104062 and DP130104459), and the Discovery Early Career Researcher Award (grant number DE150101306).

Keywords: carbon nitride · electrocatalysis · oxygen-evolution reaction · porous materials · titanium carbide

How to cite: *Angew. Chem. Int. Ed.* **2016**, *55*, 1138 – 1142
Angew. Chem. **2016**, *128*, 1150 – 1154

[1] J. Liu, Y. Liu, N. Liu, Y. Han, X. Zhang, H. Huang, Y. Lifshitz, S. T. Lee, J. Zhong, Z. Kang, *Science* **2015**, *347*, 970 – 974.
[2] J. T. Zhang, Z. H. Zhao, Z. H. Xia, L. M. Dai, *Nat. Nanotechnol.* **2015**, *10*, 444 – 452.
[3] H. Over, *Chem. Rev.* **2012**, *112*, 3356 – 3426.
[4] X. Lu, C. Zhao, *Nat. Commun.* **2015**, *6*, 6616.
[5] G. Zhang, B. Y. Xia, X. Wang, X. W. Lou, *Adv. Mater.* **2014**, *26*, 2408 – 2412.
[6] J. Ren, M. Antonietti, T. P. Fellinger, *Adv. Energy Mater.* **2015**, *5*, 1401660.
[7] G. Wu, P. Zelenay, *Acc. Chem. Res.* **2013**, *46*, 1878 – 1889.
[8] Y. Zhu, B. Zhang, X. Liu, D. W. Wang, D. S. Su, *Angew. Chem. Int. Ed.* **2014**, *53*, 10673 – 10677; *Angew. Chem.* **2014**, *126*, 10849 – 10853.
[9] W. Li, A. Yu, D. C. Higgins, B. G. Llanos, Z. Chen, *J. Am. Chem. Soc.* **2010**, *132*, 17056 – 17058.
[10] X. Yuan, X. Zeng, H. J. Zhang, Z. F. Ma, C. Y. Wang, *J. Am. Chem. Soc.* **2010**, *132*, 1754 – 1755.
[11] G. Wu, K. L. More, C. M. Johnston, P. Zelenay, *Science* **2011**, *332*, 443 – 447.
[12] X. Zou, X. Huang, A. Goswami, R. Silva, B. R. Sathe, E. Mikmeková, T. Asefa, *Angew. Chem. Int. Ed.* **2014**, *53*, 4372 – 4376; *Angew. Chem.* **2014**, *126*, 4461 – 4465.
[13] Y. Zhao, K. Watanabe, K. Hashimoto, *J. Am. Chem. Soc.* **2012**, *134*, 19528 – 19531.
[14] M. Ghidiu, M. R. Lukatskaya, M. Q. Zhao, Y. Gogotsi, M. W. Barsoum, *Nature* **2014**, *516*, 78 – 81.
[15] M. R. Lukatskaya, O. Mashtalir, C. E. Ren, Y. Dall′Agnese, P. Rozier, P. L. Taberna, M. Naguib, P. Simon, M. W. Barsoum, Y. Gogotsi, *Science* **2013**, *341*, 1502 – 1505.
[16] M. Naguib, V. N. Mochalin, M. W. Barsoum, Y. Gogotsi, *Adv. Mater.* **2014**, *26*, 992 – 1005.
[17] O. Mashtalir, M. Naguib, V. N. Mochalin, Y. Dall′Agnese, M. Heon, M. W. Barsoum, Y. Gogotsi, *Nat. Commun.* **2013**, *4*, 1716.
[18] X. Wang, K. Maeda, A. Thomas, K. Takanabe, G. Xin, J. M. Carlsson, K. Domen, M. Antonietti, *Nat. Mater.* **2009**, *8*, 76 – 80.
[19] T. Y. Ma, J. Ran, S. Dai, M. Jaroniec, S. Z. Qiao, *Angew. Chem. Int. Ed.* **2015**, *54*, 4646 – 4650; *Angew. Chem.* **2015**, *127*, 4729 – 4733.
[20] J. Zhang, M. Zhang, L. Lin, X. Wang, *Angew. Chem. Int. Ed.* **2015**, *54*, 6297 – 6301; *Angew. Chem.* **2015**, *127*, 6395 – 6399.
[21] S. Cao, J. Low, J. Yu, M. Jaroniec, *Adv. Mater.* **2015**, *27*, 2150 – 2176.
[22] Y. Wang, X. Wang, M. Antonietti, *Angew. Chem. Int. Ed.* **2012**, *51*, 68 – 89; *Angew. Chem.* **2012**, *124*, 70 – 92.
[23] M. Marszewski, S. Cao, J. Yu, M. Jaroniec, *Mater. Horiz.* **2015**, *2*, 261 – 278.
[24] Q. Peng, J. Guo, Q. Zhang, J. Xiang, B. Liu, A. Zhou, R. Liu, Y. Tian, *J. Am. Chem. Soc.* **2014**, *136*, 4113 – 4116.
[25] D. Yu, K. Goh, H. Wang, L. Wei, W. Jiang, Q. Zhang, L. M. Dai, Y. Chen, *Nat. Nanotechnol.* **2014**, *9*, 555 – 562.
[26] Y. Lee, J. Suntivich, K. J. May, E. E. Perry, Y. Shao-Horn, *J. Phys. Chem. Lett.* **2012**, *3*, 399 – 404.
[27] M. R. Gao, Y. F. Xu, J. Jiang, Y. R. Zheng, S. H. Yu, *J. Am. Chem. Soc.* **2012**, *134*, 2930 – 2933.
[28] J. Masa, W. Xia, I. Sinev, A. Zhao, Z. Sun, S. Grützke, P. Weide, M. Muhler, W. Schuhmann, *Angew. Chem. Int. Ed.* **2014**, *53*, 8508 – 8512; *Angew. Chem.* **2014**, *126*, 8648 – 8652.
[29] S. Chen, S. Z. Qiao, *ACS Nano* **2013**, *7*, 10190 – 10196.
[30] S. Chen, J. J. Duan, J. Ran, S. Z. Qiao, *Adv. Sci.* **2015**, *2*, 1400015.
[31] S. Chen, J. J. Duan, M. Jaroniec, S. Z. Qiao, *Adv. Mater.* **2014**, *26*, 2925 – 2930.
[32] H. Wang, H. W. Lee, Y. Deng, Z. Lu, P. C. Hsu, Y. Liu, D. Lin, Y. Cui, *Nat. Commun.* **2015**, *6*, 7261.
[33] Z. Lu, H. Wang, D. Kong, K. Yan, P. C. Hsu, G. Zheng, H. Yao, Z. Liang, X. Sun, Y. Cui, *Nat. Commun.* **2014**, *5*, 4345.
[34] B. Y. Xia, Y. Yan, X. Wang, X. W. Lou, *Mater. Horiz.* **2014**, *1*, 379 – 399.
[35] Q. Liu, J. Zhang, *Langmuir* **2013**, *29*, 3821 – 3828.

Received: October 22, 2015
Published online: December 2, 2015

